ACS NANO

www.acsnano.org



ARTICLE

# Developing and Investigating a Nanovibration Intervention for the Prevention/Reversal of Bone Loss Following Spinal Cord Injury

Jonathan A. Williams,* Paul Campsie, Richard Gibson, Olivia Johnson-Love, Anna Werner, Mark Sprott, Ryan Meechan, Carmen Huesa, James F. C. Windmill, Mariel Purcell, Sylvie Coupaud, Matthew J. Dalby, Peter Childs, John S. Riddell, and Stuart Reid*

Cite This: *ACS Nano* 2024, 18, 17630–17641

Read Online

ACCESS | Metrics & More | Article Recommendations | Supporting Information

**ABSTRACT:** **Osteoporosis disrupts the fine-tuned balance between bone formation and resorption, leading to reductions in bone quantity and quality and ultimately increasing fracture risk. Prevention and treatment of osteoporotic fractures is essential for reductions in mortality, morbidity, and the economic burden, particularly considering the aging global population. Extreme bone loss that mimics time-accelerated osteoporosis develops in the paralyzed limbs following complete spinal cord injury (SCI). In vitro nanoscale vibration (1 kHz, 30 or 90 nm amplitude) has been shown to drive differentiation of mesenchymal stem cells toward osteoblast-like phenotypes, enhancing osteogenesis and inhibiting osteoclastogenesis simultaneously. Here, we develop and characterize a wearable device designed to deliver and monitor continuous nanoamplitude vibration to the hindlimb long bones of rats with complete SCI. We investigate whether a clinically feasible dose of nanovibration (two 2 h/day, 5 days/week for 6 weeks) is effective at reversing the established SCI-induced osteoporosis. Laser interferometry and finite element analysis confirmed transmission of nanovibration into the bone, and microcomputed tomography and serum bone formation and resorption markers assessed effectiveness. The intervention did not reverse SCI-induced osteoporosis. However, serum analysis indicated an elevated concentration of the bone formation marker procollagen type 1 *N*-terminal propeptide (P1NP) in rats receiving 40 nm amplitude nanovibration, suggesting increased synthesis of type 1 collagen, the major organic component of bone. Therefore, enhanced doses of nanovibrational stimulus may yet prove beneficial in attenuating/reversing osteoporosis, particularly in less severe forms of osteoporosis.**

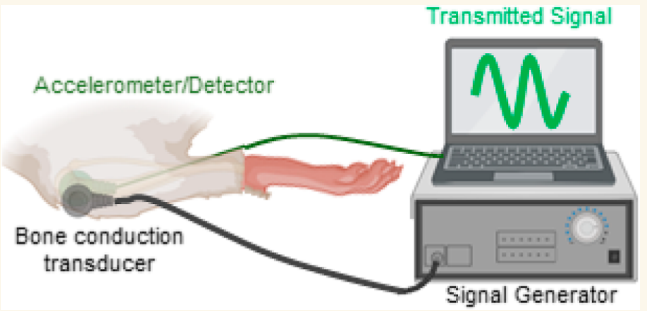


**KEYWORDS:** *vibration, biophysical stimulation, osteoporosis, microCT, mesenchymal stem cells, osteogenesis, mechanotransduction*

Osteoporosis is a worldwide public health concern of increasing importance due to an aging population.[1] It is a progressive metabolic bone disease that reflects a disruption in the fine-tuned balance between the coupled processes of bone resorption and formation, favoring resorption. Bone quantity and quality progressively depreciate, elevating susceptibility to fracture which is associated with increased morbidity, mortality, and healthcare costs.[2] In the UK, the economic burden of osteoporotic fracture is £4 billion per year, while in the US, it is $17.9 billion.[3] The prevention and treatment of these fractures is of paramount importance to society. Osteoporosis is commonly associated with aging and postmenopause. However, a very severe form of localized osteoporosis is observed at the ends of the paralyzed long bones (around the knee) following spinal cord injury (SCI), which significantly increases the risk of fragility fracture in these bones.[11] The primary mechanism behind this bone loss is a lack of muscle-driven dynamic bone stimulation.

The strategies currently available for attenuating or preventing the development of osteoporosis address the imbalance on one side, that is, attenuating bone resorption (i.e., bisphosphonates, receptor activator of nuclear factor-κB ligand antibody, and selective estrogen receptor modulators)

Received: February 13, 2024
Revised: June 13, 2024
Accepted: June 14, 2024
Published: June 26, 2024

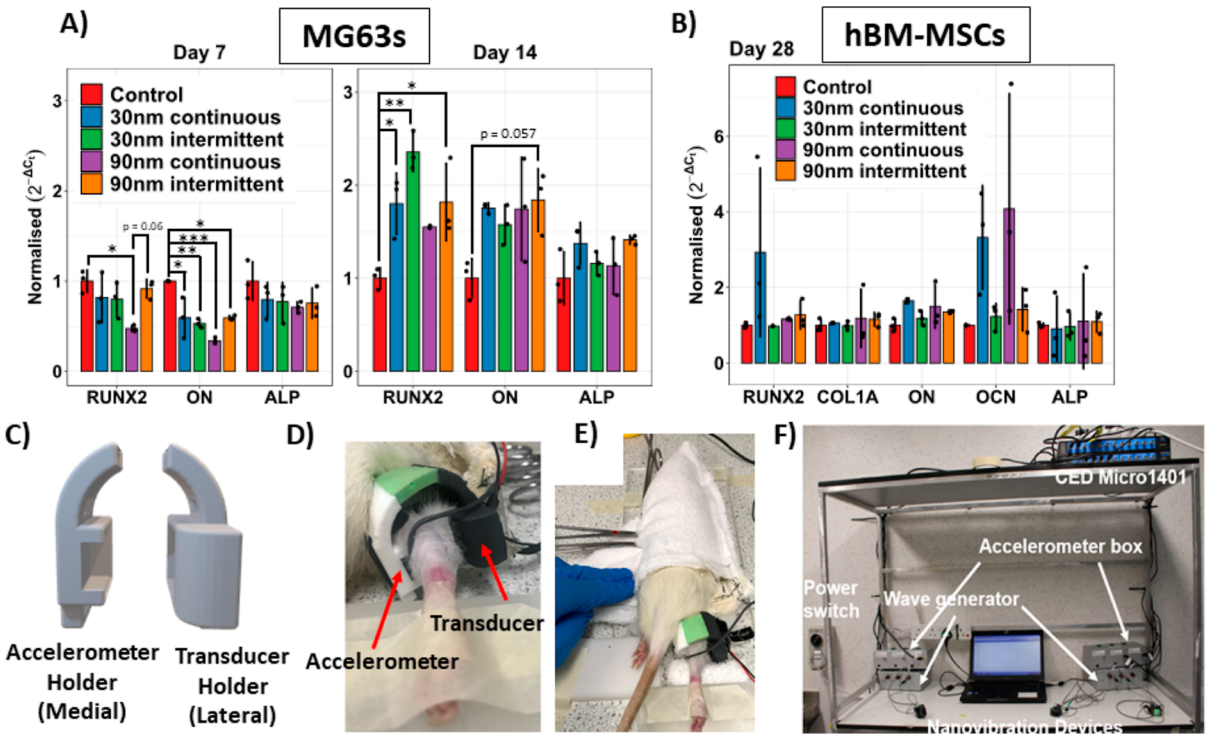


**Figure 1. Development of a wearable nanovibration delivery device. (A) 7 and 14 day qRT-PCR analysis of RUNX2, ON, and ALP transcripts in MG63 cells comparing continuous and intermittent (4 h per day) doses of nanovibration at 30 and 90 nm. (B) 28 day qRT-PCR analysis of RUNX2, COL1A, ON, OCN, and ALP in human bone marrow-derived MSCs comparing continuous and noncontinuous (4 h per day) doses of nanovibration at 30 and 90 nm. (C) CAD drawing of the 3D-printed housing of the transducer and accelerometer. (D) close-up of the nanovibration delivery device attached around the knee of the right hindlimb of a spinal cord transected rat. (E) The rat is lightly restrained within a soft towel pouch for the duration of each intervention session. (F) Overview of the complete experimental setup.**

or enhancing bone formation (i.e., teriparatide and abaloparatide).[4] This strategy is suboptimal, as of the existing microstructural deterioration, and hence fragility is not reversed in antiresorptive strategies, while anabolic strategies can partly restore microstructural deterioration, and there is some evidence that anabolic agents may reduce fracture risk more effectively.[5] Another strategy is the dual-action approach, a combination of anabolic and antiresorptive strategies either successively or together which could reduce the fracture risk more than either the strategy alone.[5]

In vitro nanoscale vibration (1 kHz, 30−90 nm amplitude) applied continuously for up to 4 weeks has been demonstrated to differentiate adult human bone marrow-derived mesenchymal stem cells (MSCs) toward the osteoblast cell linage, in both 2D culture and 3D soft-gel constructs, without the aid from osteogenic scaffolds or chemicals.[6−8] Further, osteogenesis has been confirmed by the occurrence of mineralization within soft-gel constructs.[8] Furthermore, nanovibrational stimulation of 3D cocultures of primary human osteoprogenitor and osteoclast progenitor cells simultaneously inhibits osteoclastogenesis and enhances osteogenesis.[9] This nanoscale vibration is supplied by a bespoke nanoamplitude vibrational bioreactor.[10]

To translate this technology for direct in vivo applications, the vibration delivery platform needs to be miniaturized into a noninvasive, wearable configuration. Second, a suitable animal model is needed to test its efficacy. Rat models of complete SCI are time-accelerated models of bone loss, which replicate the bone loss observed in the human SCI population.[12]

There are other vibration interventions that have applications in bone health. The two main interventions whole body vibration (WBV)[13] and low-intensity pulsed ultrasound (LIPUS),[14] each has some similarities with nanovibration that they do not have with each other. For WBV, the typical peak acceleration is between 0.3 and 0.6 g, which is comparable to the peak accelerations produced by the nanovibration used here (0.2 to 0.4 g); however, the vibration parameters are significantly different (typically <100 Hz, >1 mm). Another similarity is that the vibration is delivered continuously (not pulsed) and sinusoidally. However, the delivery mechanism of vibration to the bone (and bone cells) is decidedly different. In WBV, the stimulus is designed to be delivered to the bone through vibration-induced muscle-driven dynamic stimulation.[13] The higher frequency of nanovibration would suggest that muscle fibers are unresponsive.[15] LIPUS, on the other hand, is a targeted pulsed oscillation that penetrates into the bone tissue. Reports indicate that it has a beneficial role in fracture healing,[14,16] and recent experimental evidence indicates that it can promote MSC differentiation toward osteoblast lineages and mineralization.[17,18] The most effective parameters of LIPUS for fracture repair are at a pulse excitation frequency of 1.5 MHz, an intensity (spatial average temporal average) of 30 mW/cm$^3$, a duty cycle of 20%, and a pulse repetition frequency (PRF) of 1 kHz.[14] We note the correspondence between the PRF and the frequency of nanovibration used here. Both WBV and LIPUS have demonstrated some potential for the attenuation of mild osteoporosis in animal models.[19−22] However, this does not include SCI-induced osteoporosis, where the effects of WBV remain unclear,[23,24] while the application of LIPUS to the calcaneal bone for 6 weeks in people with SCI showed no effect.[25]



https://doi.org/10.1021/acsnano.4c02104
ACS Nano 2024, 18, 17630−17641

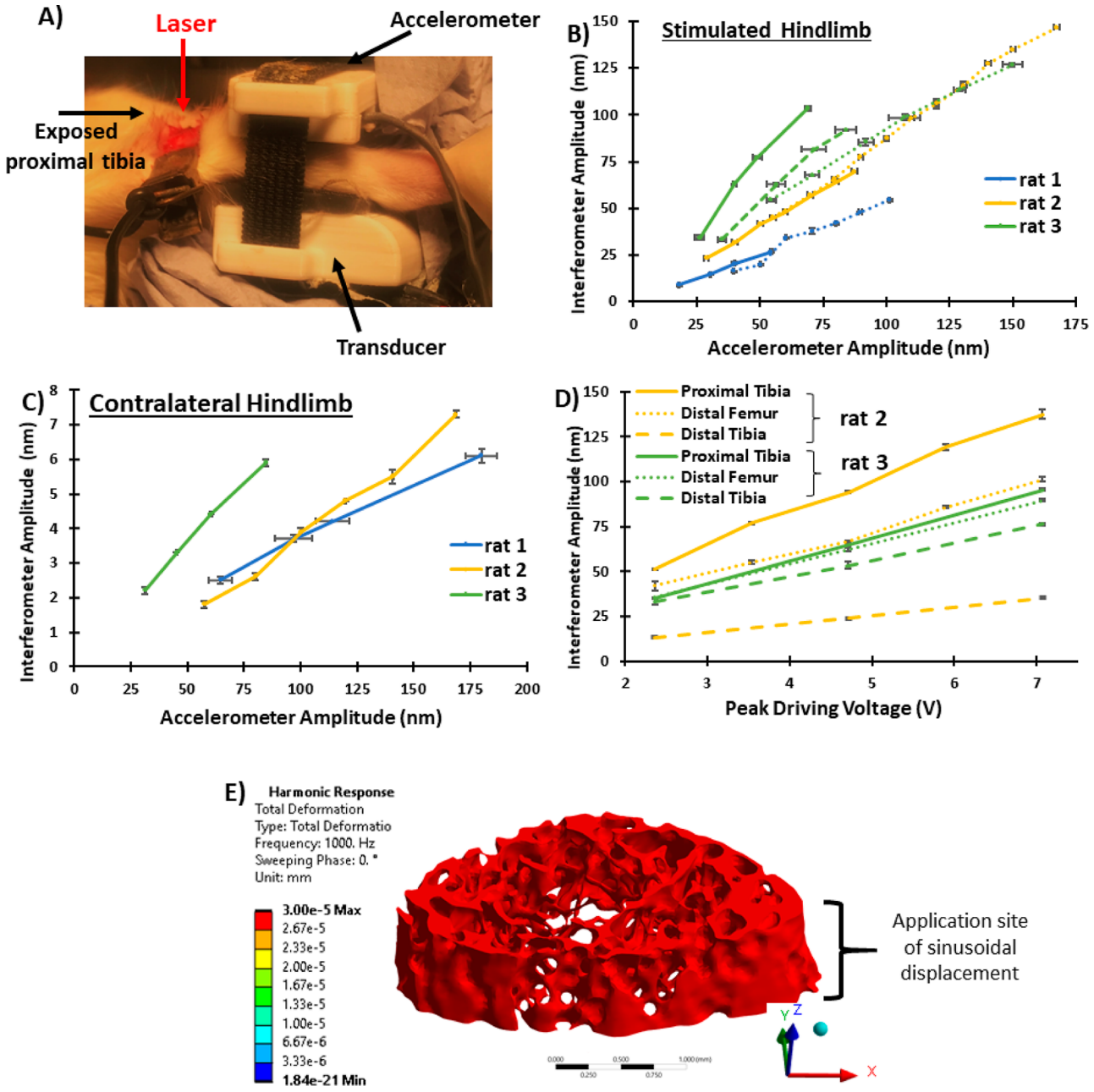


**Figure 2. Transmission of nanovibration through the bone. (A) Exposed stimulated proximal tibial laser interferometric measurement site in relation to transducer and accelerometer. (B) Plot of interferometer-derived transmitted vibration amplitude from the stimulated proximal tibial bone surface against accelerometer-derived transmitted vibration amplitude from the skin's surface, for three spinal cord transected rats. Patterned lines indicate separate measurements where the device was removed and reattached. (C) Plot of interferometer-derived (from exposed contralateral proximal tibia) and accelerometer-derived amplitude (from vibrated proximal tibia) for the different rats. (D) Plot of interferometer-derived amplitude from multiple exposed bone sites on the vibrated hindlimb. (E) Harmonic response finite element analysis (FEA) of the distal femoral metaphyseal trabecular bone, showing the predicted rigid-body-like transmission of nanovibration (minimal internal deformation). 3.00 × $10^{-5}$ mm = 30 nm. Data shown as mean ± SD.**

The overall aim of this study was to investigate the efficacy of nanovibration (1 kHz frequency, 40 or 100 nm amplitude) at reversing the SCI-induced osteoporosis observed in the paralyzed hindlimbs of completely spinal cord transected rats. The specific objectives were to (i) develop, test, and characterize the effectiveness of a device that delivers nanoamplitude vibration to the hindlimb long bones of spinal cord transected rats and (ii) determine the effect(s) that unilateral nanovibration of two different amplitudes—40 and 100 nm—has on the induced osteoporosis.

## RESULTS AND DISCUSSION

**Development of a Wearable Nanovibration Delivery Device.** In vitro nanovibration-induced bone mineralization is observed in human bone marrow-derived MSCs after 4 to 6 weeks of continuous exposure (24 h/day).[8] It is not feasible to continuously vibrate rat hindlimbs. To confirm that non-continuous (<24 h/day) nanovibration is comparable to continuous nanovibration and to determine a feasible vibration dose for in vivo applications, MG63s (an osteoblast-like cell line) and MSCs (from human bone marrow) were stimulated


https://doi.org/10.1021/acsnano.4c02104
ACS Nano 2024, 18, 17630−17641

at 1 kHz with 30 or 90 nm amplitude vibration either continuously or for 4 h per day (intermittent group) and compared to static control. After 14 days of MG63 culture, quantitative real-time PCR (qRT-PCR) revealed that the expression of the early stage osteogenic marker runt-related transcription factor 2 (RUNX2) was significantly upregulated in 30 and 90 nm amplitude intermittently vibrated groups and 30 nm amplitude continuously nanovibrated group compared to static control, indicating that a key transcription factor associated with osteoblast differentiation is upregulated (Figure 1A). Furthermore, no significant differences were observed in osteogenic gene expression between continuous or intermittent nanovibration at either time points (Figure 1A). Furthermore, after 28 days of MSC culture, no significant differences were observed in early [RUNX2 or collagen I (COL1A)] or later stage osteogenic markers [osteonectin (ON), alkaline phosphatase (ALP), or osteocalcin (OCN)] among continuous vibrated, intermittently vibrated MSCs, or nonvibrated controls (Figure 1B). This agrees with our previous work, which showed no differences in these markers after 14 days of continuous vibration, indicating that at this stage, the osteogenic process is transcriptionally complete.[8] These data suggest that an intermittent stimulation regime may be suitable to provide a comparable osteogenic stimulus in vivo.

With a valid nanovibration duration of 4 h per day, the nanovibrational bioreactor technology[10] was translated into a wearable form. Specifically, devices were developed to deliver nanoscale vibration to the MSCs within the bone marrow of the hindlimbs of awake spinal cord transected rats. The nanovibration delivery device and associated electronic systems were designed, manufactured, and validated in-house specifically for this study (Figure 1C−F). The device consisted of a bone conduction transducer (dimensions 14 mm × 21.5 mm) and an accelerometer housed within a custom-made 3D-printed plastic harness that was strapped directly to the hindlimb at the lower knee (Figure 1C−E). For more information regarding the design of the device, see Supporting Information 1.

The devices were designed to meet multiple experimental needs, such as (i) to deliver continuous sinusoidal nanoscale mechanical oscillation at a frequency of 1 kHz just below the knee to the trabecular-rich proximal tibia in the paralyzed hindlimbs of spinal cord transected rats, (ii) to measure and log the transmitted vibration, and (iii) to provide the operator in real-time the amplitude of the transmitted vibration, thus enabling adjustment of the amplitude in real-time, to ensure it remained within acceptable predefined limits. The design, fit, and optimization were refined through multiple iterations on cadavers. The advantage of using the rat model of complete spinal cord transection (SCT) as the model of bone loss is that the resulting permanent and complete hindlimb paralysis and concomitant loss of sensation meant that these rats tolerate well the direct application of a device directly to the hindlimb for a prolonged period of time. If another model of bone loss was used, then the animal would need to be anaesthetized for a duration of each 2 h intervention.[26] During the intervention, the rat was lightly restrained with a soft-towel pouch (Figure 1E). The device was attached unilaterally to the right hindlimb only (Figure 1D,E). The attachment of the device required that the hindlimb be taped down with the tibio-femoral angle at approximately 120°. Our setup enabled multiple rats to undergo the intervention simultaneously. Calibration of the devices was carried out weekly during the intervention (Supporting Information 2).

**Characterization of the Transmission of Vibration to Hindlimb Long Bones.** Prior to commencing the nanovibration intervention, the transmitted vibration amplitude at 1 kHz was measured in anesthetized rats, using laser interferometry, to confirm that suitable nanovibration parameters are deliverable to the hindlimb long bones. To optimize the delivery of nanovibration, this needed to be tested in the presence of muscle wasting, so spinal cord transected rats were used ($n = 3$). Transmitted vibration amplitudes were measured on the anteromedial surface of the right proximal tibia, which was surgically exposed under general anesthesia. For these measurements, the device's accelerometer was also attached to the skin's surface just below the exposed bone (Figure 2A), that is, two independent measures of the transmitted 1 kHz vibration amplitude were acquired simultaneously, one on the bone's surface and one on the skin's surface.

Accelerometer-derived vibration amplitude measurements of the stimulated hindlimb were overall proportional to those measured with laser interferometry at the proximal tibial bone surface (Figure 2B). However, a variation exists between the accelerometer- and interferometer-derived amplitude, for example, a 40 nm accelerometer-derived amplitude measurement translated to between 18 and 62 nm amplitude at the vibrated proximal tibial bone surface (Figure 2B). This is partially explainable by variability in the device's attachment and differences in rat hindlimb musculature between individual rats, with decreased musculature increasing the amplitude of nanovibration (data not shown). This variability is depicted for each rat with the sets of patterned lines, where between each of these measurements, the device was completely removed and then reattached (Figure 2B). These results indicate that the device must be attached to the hindlimb in a reproducible manner. The spread of nanovibration to the contralateral (i.e., nonstimulated) hindlimb was also measured at the exposed proximal tibia; importantly, it was found to be minimal (Figure 2C). All vibration amplitudes measured at the nonstimulated hindlimb were below the in vitro determined osteogenic threshold of nanovibration (20−100 nm),[7] even when the stimulated hindlimb experienced vibration amplitudes several times higher than the lower limit of this threshold (Figure 2C). This provides confidence that effective nanovibration was delivered to the directly stimulated but not to the contralateral hindlimb long bones.

Furthermore, the propagation of nanovibration along the length of the stimulated hindlimb was measured at multiple exposed bone sites (proximal and distal tibia and distal femur) with laser interferometry (accelerometer turned off) in two rats only (Figure 2D). This indicated that nanovibration was transmitted throughout the length of both the tibia and femur but diminished with distance from the transducer. Throughout the stimulated hindlimb long bones, vibration amplitudes at 1 kHz were observed that could be considered osteogenic (Figure 2D).

Finally, FEA software (ANSYS 2022 R2) was used to simulate and predict how nanovibration propagates through the trabecular bone of the distal femur by performing a harmonic response analysis with the bone structure based on $\mu$CT data. The vibration (1 kHz, 30 nm) was applied from the lateral (negative $x$) direction over a surface area that replicates the positioning and size of the vibration transducer. The simulation shows that the vibration propagates through the


https://doi.org/10.1021/acsnano.4c02104
ACS Nano 2024, 18, 17630−17641

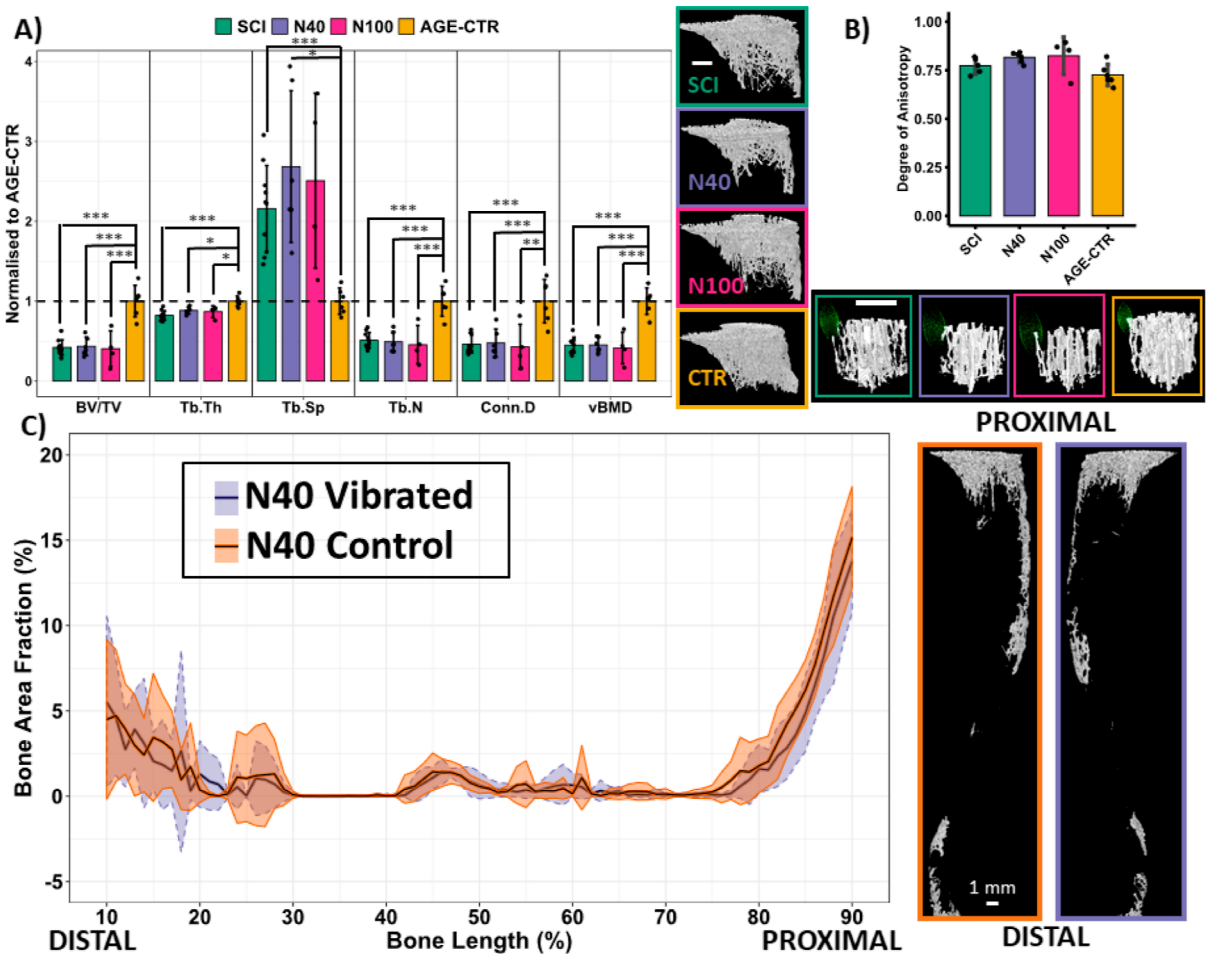


**Figure 3. Effect of nanovibration intervention on trabecular bone quantity and microarchitecture. (A) $\mu$CT-derived morphometric and densitometric analysis and representative images of the proximal tibial metaphyseal trabecular bone; the region directly stimulated by the device. The parameters measured being bone volume fraction (BV/TV), trabecular thickness (Tb.Th), trabecular separation (Tb.Sp), trabecular number (Tb.N), connectivity density (Conn.D), and volumetric bone mineral density (vBMD). (B) $\mu$CT-derived DA analysis of a trabecular bone cube within the proximal tibial metaphysis. Representative bone cube and point cloud of mean intercept lengths shown. (C) Global survey of trabecular bone area fraction for N40 rat vibrated and contralateral whole tibia (excluding epiphyses) and representative $\mu$CT-based images. White scale bars indicate 1 mm. Data shown as mean ± SD.**

trabecular bone in a rigid body-like manner, that is, it propagates with no internal stresses, causing no deformation (Figure 2E). This suggests that the vibration is fully transferred through the width of the bone with minimal attenuation.

The transmission of nanovibration to bone is then significantly different to both existing vibration interventions that have applications in bone health, principally WBV and low-intensity pulsed ultrasound (LIPUS). In WBV, the stimulus is delivered to the bone through induced muscle-driven dynamic stimulation, while the higher frequency of nanovibration would suggest that muscle fibers are unresponsive.[15] While nanovibration and LIPUS can be described as an alternating pressure wave, the higher frequency components of LIPUS indicate that it generates fluctuating pressure within the tissue,[27] and thus, reflection and attenuation significantly affect transmission. In fact, when ultrasound propagates into intact bone, up to 40% of the energy is reflected at the soft tissue-bone boundary.[28] Furthermore, greater than 80% of the remaining energy is attenuated within the first millimeter of the cortex.[28] Therefore, it can only be guaranteed that periosteal cells on the cortex's surface in the LIPUS application region are biophysically stimulated. Interestingly, dissected rat femora exposed to LIPUS exhibited a site-specific periosteal effect.[29] Specifically, only at the angle of LIPUS application, increased periosteal mineralization was observed.[29] The laser interferometric and FEA analyses performed here suggest that the much larger wavelength of nanovibration (approximately 3.5 m for bone) compared to the dimensions of the bone (<1 cm diameter of metaphysis) results in a very minimal pressure change over the bone, suggesting that the vibrational behavior of the hindlimb long bones at 1 kHz is likely rigid-body motion, with the directly stimulated tibial bone moving pistonically (in unison). Assuming rigid body vibration, this suggests that the encapsulated trabecular bone was also being nanovibrated within the osteogenic in vivo range, as verified by FEA (Figure 2E). Interestingly, LIPUS [a pulse excitation frequency of 1.5 MHz, an intensity (spatial average temporal average) of 30 mW/cm$^3$, a duty cycle of 20% and a PRF of 1 kHz] applied to the exposed bone from a fractured cadaveric human forearm has been shown to induce 1 kHz motion at the nanoscale.[30] A hypothesis has previously been made that this low frequency (1 kHz) radiation force, not the higher frequency (1.5 MHz) pulsed ultrasound, is responsible for at


https://doi.org/10.1021/acsnano.4c02104
ACS Nano 2024, 18, 17630−17641

least some of the observed biological effects.[31,32] In vitro experiments of ATDC5 chondrocytes showed that the treatment with a 1 kHz square wave at 20% duty cycle induced chondrogenesis similar to the treatment with 1.5 MHz LIPUS.[31] Furthermore, varying the PRF (1, 100, 1000 Hz) of LIPUS led to differential responses in the calcium secretion of bone marrow-derived MSCs, with increased response at the higher frequencies.[33] Cells appear sensitive to the specific PRF, which represents an acoustic (1 kHz) as opposed to an ultrasonic (1.5 MHz) component of LIPUS. The relevance of these components to the osteogenic response remains an open question.[14]

**Investigating Nanovibration to Reverse Established SCT-Induced Osteoporosis.** The rat model of complete SCT-induced osteoporosis[12,26] was used to investigate the efficacy of nanovibration at reversing established induced osteoporosis. 2 amplitudes, 30 and 90 nm, have been shown to induce osteogenesis in vitro, with the higher amplitude producing the greater osteogenic response.[7] Based on the limitations of the driving electronics, two amplitudes within a similar range to the in vitro studies were investigated, 40 nm (N40) and 100 nm (N100), as measured by the device's accelerometer. 6 weeks were allowed to pass from the time of SCT surgery to the start of the nanovibration intervention to allow time for significant trabecular bone loss, replicating that seen in chronic SCI-induced osteoporosis.[12,26] Nanovibration was then applied continuously for two 2 h sessions/day (4 h in total), 5 days/week for 6 weeks. The intervention lasted 6 weeks to coincide with the average bone turnover period in rats, which is approximately 40 days.[34] Age-matched SCT (SCI) and sham-operated control (AGE-CTR) rats were also used for comparison.

There was no difference in body mass between groups at time of surgery (Supporting Information 3). From day 3 postsurgery and onward, AGE-CTR body mass was higher than all other groups ($p < 0.05$) (Supporting Information 4). There was no difference in the body mass among N40, N100, and SCI groups at any time point postsurgery. There was no difference in gastrocnemius muscle mass at the end of the intervention between left and right hindlimbs for any group (Supporting Information 5). Also, no differences were detected in gastrocnemius mass among N40, N100, and SCI groups suggesting that nanovibration does not stimulate muscle fibers.

The trabecular bone was evaluated by microcomputed tomography ($\mu$CT) (Figure 3). In the proximal tibial metaphyseal trabecular bone, the region directly nanovibrated, and there were no significant improvements in bone quantity or microarchitecture in either N40 or N100 vibrated hindlimbs when compared to contralateral control (Supporting Information 6) or when compared to each other or with SCI rats (Figure 3A). Overall, a similar scenario is described for the proximal tibial epiphyseal and the distal femoral metaphyseal and epiphyseal trabecular bones (Supporting Information 7). Additionally, there was no change in the orientation of the trabecular bone as measured by the degree of anisotropy (DA) in the proximal tibial metaphysis trabecular bone (Figure 3B). The observation that nanovibration propagated throughout the vibrated hindlimb long bones (Figure 2D), not just in the regions directly stimulated by the transducer, motivated a global survey of the trabecular bone. However, no differences in trabecular BA/TA were observed at any point along the tibia's length; data are shown here for vibrated and contralateral control tibia of N40 rats only (Figure 3C). The cortical bone was also evaluated with $\mu$CT and mechanical testing with three-point bending. Nanovibration had no effect on the cortical bone (Supporting Information 8 and 9).

Serum bone formation and resorption were measured using procollagen type 1 *N*-terminal propeptide (P1NP) and *C*-terminal telopeptide of type I collagen (CTX), respectively, immediately following the end of the intervention (Figure 4A).

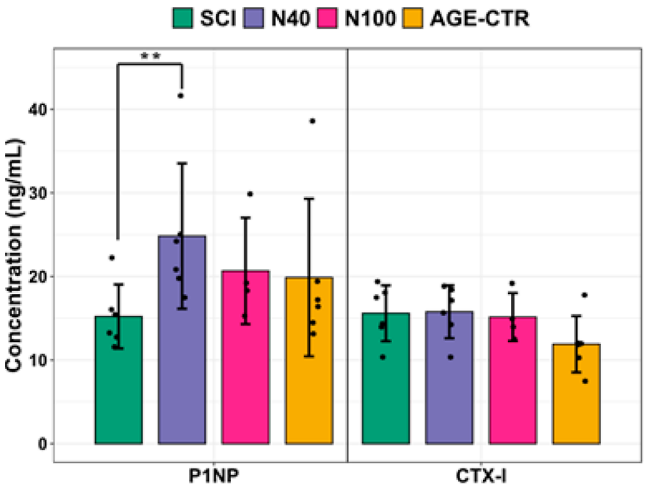


**Figure 4. Serum levels of bone turnover markers in SCI, N40, N100, and AGE-CTR groups for bone formation marker procollagen type 1 *N*-terminal propeptide (P1NP) and bone resorption marker *C*-terminal telopeptide of type I collagen (CTX). Data shown as mean ± SD ** indicates $p < 0.01$.**

The concentration of the gold standard bone formation serum marker P1NP was found to be elevated by 67% ($p < 0.01$) in the N40 group relative to the SCI group at the end of the intervention. No differences between groups were observed for the bone resorption marker CTX. These results suggest that nanovibration of certain amplitudes increases early bone formation processes (synthesis of type 1 collagen) without negatively affecting bone resorption.

**Nanovibration Delivered to Bone during Intervention.** The inclusion of a calibrated accelerometer is a key feature of the device. It was included to allow the operator to monitor and control the transmitted vibration parameters in real-time, so that vibration was continuously delivered in a consistent manner. The recorded vibration amplitude at 1 kHz from a representative 2 h intervention session and the average peak transmitted amplitude for all such sessions for a representative N40 rat are shown in Figure 5A,B, respectively. This shows that during each session, rats received a relatively consistent amplitude of vibration. Only one rat received the maximum intended duration of the intervention (Figure 5C). The remaining nanovibrated rats received a range of durations from 33 up to 97% of the intended dose. Overall, there was a larger variation in both the amplitude of transmitted nanovibration and total vibration time between N100 rats than between N40 rats (Figure 5D). The added level of precision and reproducibility that measures the transmitted vibration provides is most often missing in studies that assess vibration's ability at increasing bone mass or density. For WBV, it is recommended that the platform's vibration parameters are measured with an accelerometer prior to the start of an intervention;[35] however, this is an extremely rare occurrence. Attenuation (or amplification) of WBV, however,


https://doi.org/10.1021/acsnano.4c02104
ACS Nano 2024, 18, 17630−17641

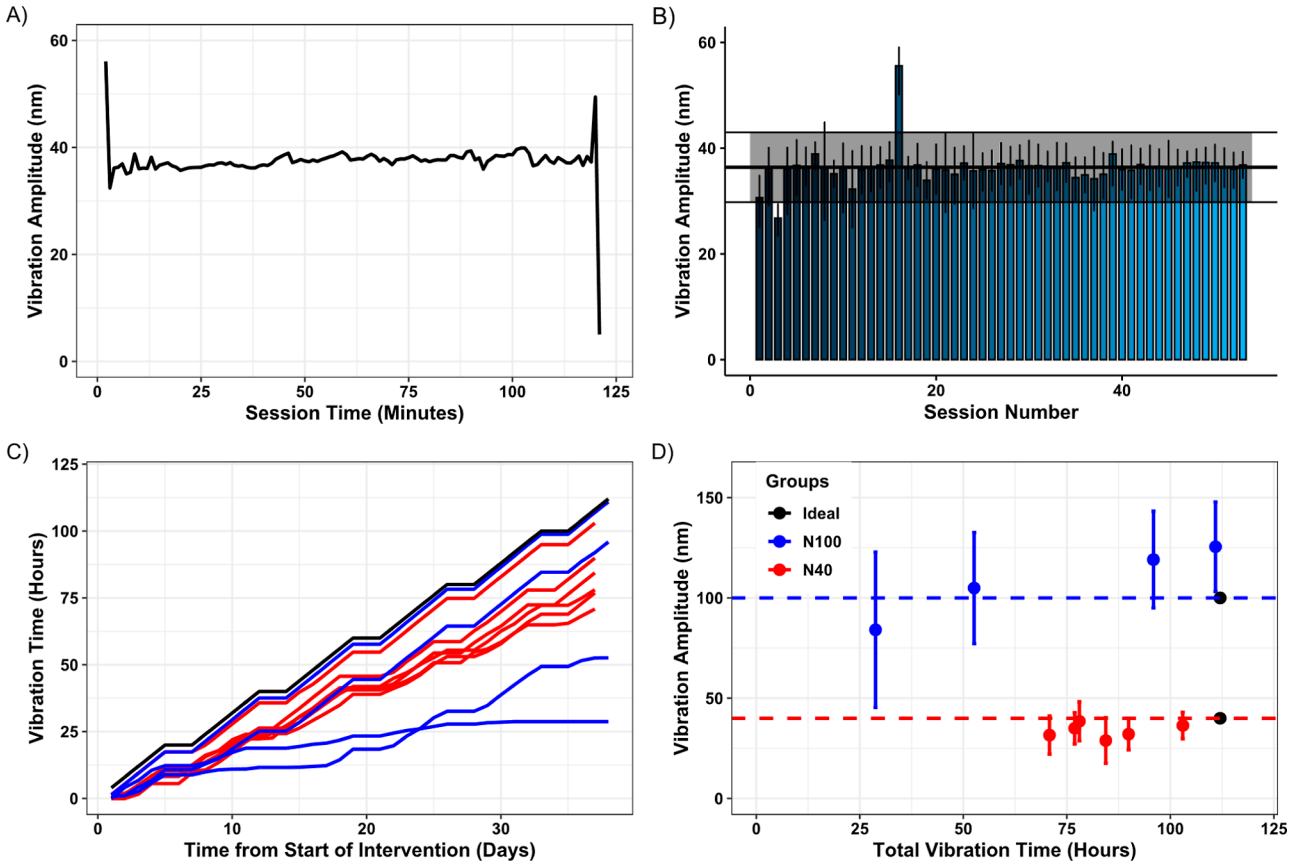


**Figure 5. Transmitted nanovibration data summary. (A) Accelerometer-derived amplitude data from a representative rat. (B) Average amplitude ± SD per nanovibration intervention session for this rat. Total average displacement ± SD throughout entire intervention is superimposed on top. (C) Cumulative plot of vibration time for each rat per day from start of intervention. (D) Plot of vibration amplitude ± SD versus overall vibration time, summarizing the nanovibration exposure for each rat, with the ideal combination of both for N40 and N100 groups plotted as black dots.**

means that it is highly probable that the vibration parameters transmitted to the bone regions under investigation are significantly different to the vibration parameters measured on the platform.[36] In our study, we observed that slight variations in the contact of the device with the rat hindlimb can lead to significant changes in the vibration dose transmitted. To our knowledge, the measurement of transmitted vibration to bone in LIPUS studies has yet to be attempted.

Despite not reversing established SCI-induced osteoporosis, this study provides evidence in support of the use of a device and experimental setup that can deliver a nanovibrational stimulus targeted specifically at the hindlimbs of a paralyzed rodent model for prolonged periods of time (>20 min) without the use of anesthesia. This has potential use for testing a variety of vibration parameters as well as other types of biophysical stimulation as therapies for bone loss.

There are several potential hypotheses to explain why this specific nanovibration intervention did not reverse existing SCI-induced bone loss. First, the vibration stimulus intensity, which is a function of duration, amplitude, and frequency, may not have been sufficient to replace SCI-induced bone loss. Further work is needed to determine if other nanovibration dose parameters provide an osteogenic effect in vivo. Second, human studies have noted that the skeletal system in patients with chronic SCI appears to be resistant to change in response to electrical muscle stimulation and WBV.[37,38] These studies concluded that preventing SCI-induced osteoporosis may be more effective than reversing the established (chronic) condition. Another consideration is whether applying the vibration for a longer overall duration (several bone remodeling cycles) would be more effective. It is also possible that an alternative model, such as ovariectomy-induced osteoporosis (OVX),[39] where the bone loss is milder and less rapid, would reveal effects not seen in the more severe SCI model. However, the main disadvantage of a model without hindlimb paralysis (e.g. OVX) is that it is challenging to design a device that awake animals will be tolerant to wearing for long enough periods of time that would deliver a sufficient dose. For these small animal models, an untargeted vibration delivery mechanism (e.g., a whole cage approach) may be required.

Our study had several limitations. Rats did not tolerate attachment of an inactive device to the contralateral control hindlimb. We also did not set up a control spinal cord transected rat group that received unilateral attachment of the device without stimulation applied. Either of these measures would have controlled for any unintended effects related to the attachment of the device itself. The second option would also have ensured that the unilateral application of nanovibration did not produce any systemic effects. However, the quantification of the transmission of nanovibration to the contralateral hindlimb (Figure 2C) provided confidence that this control hindlimb was not receiving the nanovibration stimulus. A further improvement would have been to perform dynamic histomorphometry and tartrate-resistant acid phos-


https://doi.org/10.1021/acsnano.4c02104
ACS Nano 2024, 18, 17630−17641

phatase staining to obtain further information regarding bone formation and bone resorption, respectively. This would provide more sensitive insights into the cellular response to nanovibration.

## CONCLUSIONS

In this study, a clinically feasible dose of intermittent nanovibration (two 2 h sessions per day) was identified that produces comparable effects in an osteoblast-like cell line and human bone marrow-derived MSCs to that of continuous nanovibration (Figure 1A,B). This meant that a wearable nanovibration delivery device and intervention could be developed (Figure 1C−F). Laser interferometry and FEA were utilized to demonstrate that suitable nanovibration (1 kHz, 30−90 nm) was deliverable to the trabecular bone within the proximal tibia (Figure 2). This was followed by an investigation of a nanovibration intervention for the reversal of bone loss following complete SCT in rats, which produces a very severe but reproducible bone loss within the paralyzed hindlimbs. Nanoscale amplitude vibration which inhibits osteoclastogenesis and enhances osteogenesis in vitro was delivered to the paralyzed hindlimb long bones in a continuous and consistent manner (Figure 5). This protocol did not reverse or attenuate the induced osteoporosis (Figure 3). However, blood serum analysis indicated an elevated concentration of the bone formation marker P1NP in rats receiving the 40 nm amplitude intervention (Figure 4). This suggests that nanovibration increased the synthesis of the main component of the organic matrix of bone—type 1 collagen. Other doses of nanovibration stimulus may yet prove productive at attenuating or reversing bone loss, particularly in less severe types of osteoporosis.

## METHODS

**Cell Culture.** Human bone marrow MSCs (PromoCell) and MG63 cells (ECACC) were cultured separately in Dulbecco's modified essential medium (DMEM, Sigma), supplemented with 10% (v/v) fetal bovine serum (FBS, Sigma), 1% nonessential amino acid (MEM NEA, Gibco), and 2% antibiotics (penicillin/streptomycin, Sigma). MSCs were used at passage 4 and MG63s were used at passage <20. MG63 cells were seeded at 1136 cells/cm$^2$ and MSCs were used at 4000 cells/cm$^2$ into 96-well plates. MG63s were seeded at a lower density to avoid overgrowth by day 14. Cells were incubated at 37 °C with 5% $CO_2$, and media were changed every 3 days.

96-well plates were magnetically coupled to the bespoke nanoamplitude vibrational bioreactor to receive nanovibration stimulation. Nanovibration stimulation started 24 h following seeding to allow cells to adhere. Control cells were cultured without nanovibration stimulation. Nanovibrated cells were either continuously nanovibrated at an amplitude of 30 or 90 nm or intermittently vibrated at 30 or 90 nm for 4 h per day (between 12:00 and 16:00) to replicate the time scale utilized within the in vivo experiments. These conditions were applied to MG63s for 7 and 14 days and to MSCs for 28 days.

**Quantitative Real-Time PCR.** Subsequently, cells were lysed, RNA was extracted, and reverse transcription was performed using TaqMan Fast Advanced Cells-to-CT Kit (Thermo Fisher) according to the manufacturer's instructions. Forward and reverse primers for qRT-PCR are shown in Table 1. The housekeeping gene used was GAPDH. qRT-PCR was then performed using the QuantStudio 5 real-time PCR system (Thermo Fisher Scientific). $\Delta C_t$ values were calculated using GAPDH and compared between treatment groups. Three biological replicates were used per group, and three technical replicates per sample were used.

**Nanovibration Delivery Device Design.** Nanovibration delivery devices and associated electronic systems were designed, manufactured, and validated in-house specifically for this study (Figure 1C−F). The device consisted of a bone conduction transducer (Adafruit Industries, New York) and accelerometer (ACH-01, TE Connectivity, Schaffhausen, Switzerland) housed within a custom-made, 3D-printed plastic harness (PLA, 70% infill, resolution 300 $\mu$m) (Figure 1C,D). The design featured two holders one for the transducer and other for the accelerometer. To prevent unwanted vibrations traveling through the device, a strip of foam material (PORON Vive, Algeos, Liverpool) was glued between the two holders. Each holder contained a slot that allowed the passage of an elasticated strap. The strap had hook and loop fastener at its ends, allowing the transducer and accelerometer to remain in firm contact with the lateral and medial sides of the rat hindlimb just below the knee (Figure 1D,E), respectively.

**Table 1. Assay IDs Used in qRT-PCR**

| | TaqMan assay ID | MG63 | MSC |
|---|---|---|---|
| GAPDH | Hs02786624_g1 | √ | √ |
| RUNX2 | Hs01047973_m1 | √ | √ |
| ON | Hs00234160_m1 | √ | √ |
| COL1A | Hs00164004_m1 | | √ |
| OCN | Hs01587814_g1 | | √ |
| ALP | Hs01029144_m1 | √ | √ |

A wave generator circuit was designed, constructed, and tested to drive the transducer top plate at 1 kHz, and the amplitude of vibration was controlled by the operator with a rotatory potentiometer (See Supporting Information 1 for further details). Accelerometer circuitry was also designed, constructed, and tested to amplify and record the nanoscale vibration detected by the accelerometer. Furthermore, this signal was sent to a Cambridge Electronic Design (CED) Micro 1401 data acquisition unit (CED Limited, Cambridge, UK) and connected to a PC, where all the raw data of the measurement session, as well as the average peak value of the signal over each one-minute time scale, were recorded by Spike2 software (associated with CED Limited hardware) on the PC. The Spike2 script also indicated to the operator in real-time whether the acceleration (converted to displacement) measured was within the acceptable limits by plotting data colored red if it was not within the limits and green if it was. These predefined limits were 35−45 and 90−100 nm for N40 and N100 groups, respectively. Prior to use in the intervention, accelerometers were calibrated against an in vitro nanoamplitude vibration plate, which was itself calibrated using laser interferometry[10] (See Supporting Information 2 for further details). The wave generator and accelerometer circuitry were housed in sets of three, giving the capability of nanovibrating multiple rats simultaneously (Figure 1F).

**Interferometric Measurement.** Measurements of the transmitted vibration amplitude were performed on four SCI rats (3 weeks postsurgery), prior to commencing the intervention to confirm that suitable nanovibration parameters were delivered to hindlimb long bones. Under general anesthesia, rat hindlimbs were shaved, and the device was attached. The anteromedial surface of the right proximal tibia and distal femur were surgically exposed. Retroreflective tape was then attached directly to these exposed bone surfaces. Single point laser interferometry (Model SP-S SIOS Me$\beta$technik GmbH, Ilmenau, Germany) was then performed to measure the amplitude of vibration at 1 kHz from the tape, while the hindlimb was undergoing direct nanovibration from the device. The amplitude of vibration of the transducer top plate was controlled by the operator with the rotatory potentiometer incrementally increased from the lowest to the highest setting. Simultaneously, accelerometer-derived vibration amplitudes from the skin surface just below the exposed proximal tibia were simultaneously acquired (See Figure 2). Multiple measurements were made per rat to observe the expected variation. The spread of nanovibration was also measured along the length of the long bones by exposing other bone sites (midfemur, distal femur, midtibia, and distal tibia). Propagation of nanovibration to the contralateral hindlimb was also monitored by measuring the vibration amplitude at the exposed anteromedial surface of the contralateral proximal tibia.



https://doi.org/10.1021/acsnano.4c02104
ACS Nano 2024, 18, 17630−17641

**Rat Model of Complete SCT.** Twenty-six male Sprague−Dawley rats weighing 201−225 g were acquired from Charles River Laboratories (Kent, UK). Rats were housed in threes or fours, in a temperature-controlled room under a 12 h light−dark cycle, with ad libitum access to food and water. All experimental procedures were approved by the Ethical Review Panel of the University of Glasgow and carried out in accordance with the Animals (Scientific Procedures) Act 1986.

Following 1 week of acclimatization, rats were randomly assigned into two groups: a SCT group ($n$ = 20) or sham surgery (SHAM) group ($n$ = 6). SCT rats underwent transection of the spinal cord at T9, and in the SHAM group, the spinal cord was exposed but not transected. This procedure has been described previously.[12] Briefly, the spinal cord of anesthetized rats was exposed by laminectomy at the T9-T10 level. The transection was produced by making a small hole in the dura and cutting the spinal cord transversely at two locations, approximately 1 mm apart. The spinal cord tissue between the transections was removed by aspiration, and the completeness of the transection was confirmed visually through an operating microscope. Rats received buprenorphine (0.05 mg/kg s.c.) and carprofen (5 mg/kg s.c.) the morning of and morning after surgery. Saline (3−5 mL s.c.) and enrofloxacin (5 mg/kg s.c.) were given for 7 days postsurgery. The bladders of SCI rats were manually expressed 3-times per day until spontaneous voiding returned.

Starting 3 days postsurgery, once sufficiently recovered, SCT rats underwent pouch-training sessions thrice weekly for the first 6 weeks postsurgery to acclimatize to the experimental setup. This involved lightly restraining the rat inside a soft towel pouch, which allowed for access to the hindlimbs (Figure 1E). The length of pouch training sessions was increased weekly from 15, 30, and 60 to 120 min. These training sessions allowed identification of the SCT rats most suitable for undergoing the unilateral nanovibration intervention. After 6 weeks of pouch training, the rats suitable for receiving nanovibration were selected. Suitable rats were those that tolerated being pouched for 2 h per session. In total, ten SCT rats received targeted nanovibrational stimulation. These rats were further subdivided into two nanovibration groups according to vibration amplitude: 40 nm (N40) and 100 nm (N100) groups. SCT rats not selected for vibration were assigned to the SCI control group (SCI), and the rats that received SHAM surgery were assigned to the age-matched control group (AGE-CTR). The four groups that make up this study are N40 ($n$ = 6), N100 ($n$ = 4), SCI ($n$ = 10), and AGE-CTR ($n$ = 6). Three further SCT rats were used to confirm transmission of nanovibration using laser interferometry (as described above).

**Microcomputed Tomography.** Trabecular and cortical bone morphology and densitometry of the tibia and femur from both hindlimbs were assessed with ex vivo micro-computed tomography ($\mu$CT) using the Bruker SkyScan 1172 scanner (Kontich, Belgium) with a Hamamatsu 80 kVp/100 $\mu$A X-ray tube at 10 $\mu$m isotropic voxel size, as previously described.[40] All long bones were scanned with the following settings. 70 kVp X-ray tube voltage, 100 $\mu$A X-ray tube current, 470 ms exposure time, 2000 × 1332 pixels per image, with a frame averaging of 2, and a 0.4° rotation step for a total of 180° with a 0.5 mm thick aluminum filter. At this voxel size, each long bone was fully captured with either 4 or 5 subscans which are stitched together with averaging during reconstruction in NRecon software (Version 1.6.9.18, Kontich, Belgium).

Three volumes of interest (VOIs) were selected for each tibia and femur in CT-Analyzer software (version 1.18.8.0+). For the tibiae, these were the proximal epiphyseal trabecular bone, proximal metaphyseal trabecular bone, and mid-diaphyseal cortical bone. For the femora, these were the distal epiphyseal trabecular bone, distal metaphyseal trabecular bone, and mid-diaphyseal cortical bone. For epiphyseal trabecular bone, the entire epiphysis enclosed by the growth plate was selected. A percentage-based selection approach was used for the remaining VOIs. The metaphyseal trabecular VOI began at an offset of 2.5% bone length from the growth plate reference point and extended for 5% bone length. The cortical mid-diaphyseal VOIs extended between 47.5 and 52.5% bone length from the proximal end. Epiphyseal trabecular bone was manually segmented from the encapsulating cortical shell. Metaphyseal trabecular and cortical bone VOIs were automatics segmented using a morphological escalation in CT-Analyzer, as previously described.[26]

Morphometric analysis was performed on these VOIs after binarization via a global threshold (90/255) and subsequent despeckling for noise removal in a CT-Analyzer. Trabecular measures included bone volume fraction (BV/TV), trabecular thickness (Tb.Th), trabecular number (Tb.N), trabecular separation (Tb.Sp), and connectivity density (Conn.D) as per (Bouxsein et al., 2010).[41] Cortical measures included cortical thickness (Ct.Th), cortical bone volume (Ct.V), total volume enclosed by the periosteum (Tt.V), marrow volume (Ma.V), cortical volume fraction (Ct.V/Tt.V), second polar moment of area (J), cortical bone surface area to volume ration (BS/BV) as per Bouxsein et al., 2010 and eccentricity (Ecc). Trabecular vBMD, and cortical bone tissue mineral density (TMD) were determined after calibration using two scanner manufacturer provided 4 mm diameter calibration hydroxyapatite phantoms, with known densities of 0.25 and 0.75 g cm$^{-3}$.

Following morphometric analysis in the CT-Analyzer, the DA was calculated in BoneJ2.[42] DA is a measure used to quantify the predominant orientation/directionality of trabecular bone. To obtain meaningful values, it must be applied to a sample of a larger whole (sub-VOI). DA was determined for a cubic sub-VOI with side length 1.2 mm taken from the proximal tibial metaphyseal trabecular bone VOI. This size of cube was chosen to ensure that the sub-VOI contained at least 5 intratrabecular lengths.[41] Consistent placement of the cubic sub-VOI was crucial for obtaining meaningful results, and small variation in location would mean that biomechanically homologous regions were not being compared between bones. Consistent placement of the cubic sub-VOI was ensured by spatially aligning all data sets in a semiautomated fashion using a procedure termed coregistration in DataViewer software (Version 1.7.4.2, Kontich, Belgium), as per published methods.[40] The cubic VOI started 1 mm distal of the proximal tibial growth plate to ensure that (i) it only contained secondary spongiosa and (ii) its location lay within the region directly stimulated by the nanovibration delivery device. The location for the cubic sub-VOI was within the lateral segment of the proximal tibial metaphysis; it was the only region that satisfied all the above requirements (see Supporting Information 10). The MIL algorithm was used to calculate DA.[43] Briefly, parallel lines from different directions are drawn through the whole cubic sub-VOI. Each individual line is sampled to find points where there is a phase change in the binarized data set—changes from background to foreground (bone). After all lines are sampled in a given direction, a MIL vector is obtained for that direction, the length of which is equal to the total length of all the lines in that direction divided by the total number of phase changes detected. This is repeated for all the directions. Each MIL vector is then plotted around the origin. An ellipsoid is then fitted to this MIL vector space. It is the radii of the ellipsoid ($a$, $b$ and $c$) that determined DA to be

$$\mathrm{DA} = 1 - \frac{1}{c^2} / \frac{1}{a^2}$$

where $a \leq b \leq c$. The following parameters were used for the analysis; the number of directions was set to 2000, lines per direction was set to 10,000, and the sampling increment was set to 1.73. The DA algorithm is stochastic because the directions of parallel lines are randomly chosen, which means exactly repeatable results are not guaranteed. The algorithm was run 5 times per sub-VOI to establish the DA. Note that a DA of 0 indicates that the trabecular bone data set is completely isotropic, while a DA of 1 indicates that it contains a very prominent overall orientation.

Also subsequent to the morphometric analysis, a survey of the 2D trabecular morphometry was conducted along the entire length of each tibia and femur, as per published methods,[40] to compliment the site-specific 3D trabecular morphometric analysis and to quantify the regions not typically quantified by that approach, and to determine whether there were structural effects of nanovibration that would otherwise have been missed. Briefly, the first 10% bone length proximal and last 10% distal of the tibia and the first 15% proximal


https://doi.org/10.1021/acsnano.4c02104
ACS Nano 2024, 18, 17630−17641

and last 15% distal of the femur were excluded from the analysis so to avoid inclusion of the complex geometry of the epiphyses. The remaining trabecular structures were automatically segmented from the cortical bone in the CT-Analyzer. 2D slice-by-slice analysis of the trabecular bone area fraction (BA/TA) was performed in the CT-Analyzer. BA/TA is defined as the ratio of the total number of pixels representing trabecular bone to the total number of marrow cavity pixels. BA/TA was determined for every single slice in the binarized, segmented trabecular data set and plotted as a function of bone length. If interesting effects were noticed in specific regions, then these regions of interest could then be further investigated with the standard analysis described above.

**Finite Element Modeling.** A $\mu$CT scan of the distal femoral metaphyseal trabecular bone from a representative SHAM group was used to create a 3D model (STL file) in a CT-Analyzer. This surface mesh was imported into ANSYS SpaceClaim and was cleaned up using the built-in autofix function, reducing the number of facets, and shrink-wrapping the body. Multiple iterations of these procedures were required to produce a model that was processable as a volumetric mesh. Harmonic analysis was performed on this mesh to evaluate its structural response when subjected to nanovibration [sinusoidally varying displacement (30 nm, 1 kHz)]. The material properties of the bone were assigned as homogeneous, isotropic, and linear elastic materials. Specifically, density was acquired from the trabecular bone TMD of the $\mu$CT scan, a Young's modulus of 19.72 GPa, derived from TMD using an empirically derived equation,[44] and a Poisson's ratio of 0.3 were used. A displacement was applied to the model in the transverse direction, with a contact area comparable to that of the surface area of the transducer. Elastic supports were assigned to the top and bottom surfaces to simulate adjacent bone structures, and a foundational stiffness of 1 N/mm$^3$ was used. The model was then subjected to the harmonic analysis.

**Three-Point Bend Mechanical Testing.** Following $\mu$CT scanning, all femora underwent loading to failure in a three-point bend test. Femora were oriented in the anterior-posterior position (with the anterior surface in tension). The actuator head was lowered at a rate of 1 mm min$^{-1}$ using a servohydraulic testing machine with a 2 kN load cell (Zwick/Roell z2.0, August-Nagel-Strasse 11, Ulm, Germany). Femora were preloaded to 10 N and allowed to adapt for 10 s before being tested to failure. Load and actuator displacement were recorded at a sampling rate of 100 Hz, using testXpert II (Version 3.61) software. A 15 mm span length was used. The whole-bone structural properties such as maximum load, stiffness, and absorbed energy were obtained, and the tissue-level mechanical properties such as elastic modulus and ultimate stress were calculated from the equations of beam theory.[45]

**Serum Bone Formation and Resorption Markers.** Serum markers of bone formation and resorption were measured using rat/mouse procollagen type 1 *N*-terminal propeptide (P1NP) and RatLaps C-terminal telopeptide of type I collagen (CTX-I) enzyme immunoassay kits (Immunodiagnostic Systems, Tyne & Wear, UK), respectively, at the time of euthanasia for all rats within the nanovibration study ($n$ = 26). The assays were performed following the manufacturer's instructions.

**Statistics.** To determine differences in gastrocnemius muscle mass, $\mu$CT-derived morphometric and densitometric parameters and three-point bend-derived mechanical properties between left and right tibiae and femora within the same group of rats, first normality was assessed using the Shapiro–Wilk test on residues and by visually inspecting the spread of data. If data could be assumed normally distributed, then the parametric paired $t$-test was performed. If data could not be assumed normally distributed, then the nonparametric paired samples Wilcoxon test was performed. Multiple group comparisons were performed on right hindlimb tibiae and femora only. First, normality was assessed using the Shapiro–Wilk test on residues and by visually inspecting the spread of data. Homogeneity of variances was tested using Levene's test. Data were assumed normally distributed, and homogeneity of variances was tested using one-way analysis of variance (ANOVA) with Tukey's HSD posthoc. In the cases of normally distributed data but with nonhomogeneous variances, ANOVA was performed with Games Howell post hoc test, while data assumed to not be normally distributed data were tested with independent samples Kruskal–Wallis test for multiple groups with Dunn's post-hoc test. To determine differences between left and right tibiae (and left and right femora) within the same group of rats, normality was assessed using the Shapiro–Wilk test on residues first and then by visually inspecting the spread of data. If data could be assumed normally distributed, then the parametric paired $t$-test was performed. If data could not be assumed normally distributed, then the nonparametric paired samples Wilcoxon test was performed. A mixed-model repeated measures ANOVA was used to assess body mass at multiple time points within the same rats. Significance was defined as $p < 0.05$. For qRT-PCR data, Dixon's Q test for outliers was performed with significance level set to $p < 0.15$, and subsequently, one-way ANOVA with Tukey's HSD posthoc was performed. All results are expressed as mean ± standard deviation. All statistical analyses were performed in R (Version 3.6.1).

## ASSOCIATED CONTENT

### Supporting Information

The Supporting Information is available free of charge at https://pubs.acs.org/doi/10.1021/acsnano.4c02104.

Description of the nanovibration delivery device electronic systems; calibration of accelerometers; initial and end rat body mass; rat body mass throughout intervention; gastrocnemius muscle mass at the end of intervention; $\mu$CT analysis of proximal tibial metaphyseal and epiphyseal trabecular bone, distal femoral metaphyseal, and epiphyseal trabecular bone; three-point bend-determined whole-bone and material-level mechanical properties of tibial mid-diaphyseal cortical bone; and location of trabecular bone volume of interest for DA analysis (PDF)

Harmonic response finite element analysis (FEA) of the distal femoral metaphyseal trabecular bone, showing the predicted rigid-body-like transmission of nanovibration (minimal internal deformation) (AVI)

## AUTHOR INFORMATION


### Corresponding Authors

**Jonathan A. Williams** − *Centre for the Cellular Microenvironment, Department of Biomedical Engineering, Wolfson Centre, University of Strathclyde, Glasgow G4 0NW, U.K.; School of Psychology and Neuroscience, College of Medical, Veterinary and Life Sciences, University of Glasgow, Glasgow G12 8QQ, U.K.; Scottish Centre for Innovation in Spinal Cord Injury, Queen Elizabeth National Spinal Injuries Unit, Queen Elizabeth University Hospital, Glasgow G51 4TF, U.K.;* orcid.org/0000-0002-9828-4886; Email: jonathan.williams@strath.ac.uk

**Stuart Reid** − *Centre for the Cellular Microenvironment, Department of Biomedical Engineering, Wolfson Centre, University of Strathclyde, Glasgow G4 0NW, U.K.;* Email: stuart.reid@strath.ac.uk

### Authors

**Paul Campsie** − *Centre for the Cellular Microenvironment, Department of Biomedical Engineering, Wolfson Centre, University of Strathclyde, Glasgow G4 0NW, U.K.*

**Richard Gibson** − *Centre for the Cellular Microenvironment, Department of Biomedical Engineering, Wolfson Centre, University of Strathclyde, Glasgow G4 0NW, U.K.*

**Olivia Johnson-Love** − *Centre for the Cellular Microenvironment, Department of Biomedical Engineering,*




https://doi.org/10.1021/acsnano.4c02104
*ACS Nano* 2024, 18, 17630−17641

*Wolfson Centre, University of Strathclyde, Glasgow G4 0NW, U.K.*

**Anna Werner** − *Centre for the Cellular Microenvironment, Department of Biomedical Engineering, Wolfson Centre, University of Strathclyde, Glasgow G4 0NW, U.K.*

**Mark Sprott** − *Centre for the Cellular Microenvironment, Institute of Molecular, Cell and Systems Biology, College of Medical, Veterinary and Life Sciences, University of Glasgow, Glasgow G12 8QQ, U.K.*

**Ryan Meechan** − *Centre for the Cellular Microenvironment, Department of Biomedical Engineering, Wolfson Centre, University of Strathclyde, Glasgow G4 0NW, U.K.*

**Carmen Huesa** − *Institute of Infection, Immunity and Inflammation, College of Medical, Veterinary and Life Sciences, University of Glasgow, Glasgow G12 8QQ, U.K.*

**James F. C. Windmill** − *Department of Electronic and Electrical Engineering, Royal College Building, University of Strathclyde, Glasgow G1 1XW, U.K.*; orcid.org/0000-0003-4878-349X

**Mariel Purcell** − *Scottish Centre for Innovation in Spinal Cord Injury, Queen Elizabeth National Spinal Injuries Unit, Queen Elizabeth University Hospital, Glasgow G51 4TF, U.K.*

**Sylvie Coupaud** − *Centre for the Cellular Microenvironment, Department of Biomedical Engineering, Wolfson Centre, University of Strathclyde, Glasgow G4 0NW, U.K.; Scottish Centre for Innovation in Spinal Cord Injury, Queen Elizabeth National Spinal Injuries Unit, Queen Elizabeth University Hospital, Glasgow G51 4TF, U.K.*

**Matthew J. Dalby** − *Centre for the Cellular Microenvironment, Institute of Molecular, Cell and Systems Biology, College of Medical, Veterinary and Life Sciences, University of Glasgow, Glasgow G12 8QQ, U.K.*; orcid.org/0000-0002-0528-3359

**Peter Childs** − *Centre for the Cellular Microenvironment, Department of Biomedical Engineering, Wolfson Centre, University of Strathclyde, Glasgow G4 0NW, U.K.*

**John S. Riddell** − *School of Psychology and Neuroscience, College of Medical, Veterinary and Life Sciences, University of Glasgow, Glasgow G12 8QQ, U.K.*

Complete contact information is available at: https://pubs.acs.org/10.1021/acsnano.4c02104

### Author Contributions

Data collected in this study are accessible at 10.15129/0b2d2d47-f4c9-40a6-a2ad-72565a740e37. $\mu$CT data sets can be made available on reasonable request.

### Author Contributions

J.A.W, S.C., M.J.D, J.S.R, and S.R. conceived the experiments. J.A.W., P.C., R.G., O.J-L, A.W., M.S., R.M., C.H., and J.S.R. performed the experiments. J.A.W., P.C., P.G.C, C.H., J.F.C.W., M.P., M.J.D., and P.C. provided materials and expertise. M.P., S.C., J.S.R., and S.R. acquired funding. J.A.W, O.J-L, A.W., and R.M. analyzed the data. J.A.W. wrote the manuscript and prepared the figures. All authors have given approval to the final version of the manuscript.

### Notes

The authors declare no competing financial interest.

A preprint of this manuscript was made available prior to publication: Jonathan A. Williams, Paul Campsie, Richard Gibson, Olivia Johnson-Love, Anna S Werner, Mark Sprott, Ryan Meechan, Carmen Huesa, James F.C. Windmill, Mariel Purcell, Sylvie Coupaud, Matthew J. Dalby, Peter G. Childs, John S. Riddell and Stuart Reid, "Developing and Investigating a Nanovibration Intervention for the Prevention/Reversal of Bone Loss Following Spinal Cord Injury." 2024, 02.12.578,222. bioRxiv. 10.1101/2024.02.12.578222 (Accessed 05/31/2024).

## ACKNOWLEDGMENTS

This study was supported by funding provided by the Science and Technology Facilities Council (STFC) Challenge Led Applied Systems Programme (ST/S000968/1) and (ST/S000852/1) and support from the Universities of Strathclyde and Glasgow. R.G. was supported by the Engineering and Physical Sciences Research Council (EPSRC) Centre for Doctoral Training in Medical Devices & Health Technologies (EP/L015595/1). S.R. is supported by a Royal Society Industry Fellowship (INF\R1\201072).

## REFERENCES

(1) Christensen, K.; Doblhammer, G.; Rau, R.; Vaupel, J. W. Ageing Populations: The Challenges Ahead. *Lancet* **2009**, *374* (9696), 1196−1208.

(2) Shuid, A. N.; Khaithir, T. M. N.; Mokhtar, S. A.; Mohamed, I. N. A Systematic Review of the Outcomes of Osteoporotic Fracture Patients after Hospital Discharge: Morbidity, Subsequent Fractures, and Mortality. *Ther. Clin. Risk Manage.* **2014**, *10*, 937−948.

(3) Clynes, M. A.; Harvey, N. C.; Curtis, E. M.; Fuggle, N. R.; Dennison, E. M.; Cooper, C. The Epidemiology of Osteoporosis. *Br. Med. Bull.* **2020**, *133* (1), 105−117.

(4) Langdahl, B. L. Overview of Treatment Approaches to Osteoporosis. *Br. J. Pharmacol.* **2021**, *178* (9), 1891−1906.

(5) Seeman, E.; Martin, T. J. Antiresorptive and Anabolic Agents in the Prevention and Reversal of Bone Fragility. *Nat. Rev. Rheumatol.* **2019**, *15* (4), 225−236.

(6) Nikukar, H.; Reid, S.; Tsimbouri, P. M.; Riehle, M. O.; Curtis, A. S. G.; Dalby, M. J. Osteogenesis of Mesenchymal Stem Cells by Nanoscale Mechanotransduction. *ACS Nano* **2013**, *7* (3), 2758−2767.

(7) Orapiriyakul, W.; Tsimbouri, M. P.; Childs, P.; Campsie, P.; Wells, J.; Fernandez-Yague, M. A.; Burgess, K.; Tanner, K. E.; Tassieri, M.; Meek, D.; Vassalli, M.; Biggs, M. J. P.; Salmeron-Sanchez, M.; Oreffo, R. O. C.; Reid, S.; Dalby, M. J. Nanovibrational Stimulation of Mesenchymal Stem Cells Induces Therapeutic Reactive Oxygen Species and Inflammation for Three-Dimensional Bone Tissue Engineering. *ACS Nano* **2020**, *14* (8), 10027−10044.

(8) Tsimbouri, P. M.; Childs, P. G.; Pemberton, G. D.; Yang, J.; Jayawarna, V.; Orapiriyakul, W.; Burgess, K.; González-García, C.; Blackburn, G.; Thomas, D.; Vallejo-Giraldo, C.; Biggs, M. J. P.; Curtis, A. S. G.; Salmerón-Sánchez, M.; Reid, S.; Dalby, M. J. Stimulation of 3D Osteogenesis by Mesenchymal Stem Cells Using a Nanovibrational Bioreactor. *Nat. Biomed. Eng.* **2017**, *1* (9), 758−770.

(9) Kennedy, J. W.; Tsimbouri, P. M.; Campsie, P.; Sood, S.; Childs, P. G.; Reid, S.; Young, P. S.; Meek, D. R. M.; Goodyear, C. S.; Dalby, M. J. Nanovibrational Stimulation Inhibits Osteoclastogenesis and Enhances Osteogenesis in Co-Cultures. *Sci. Rep.* **2021**, *11* (1), 22741.

(10) Campsie, P.; Childs, P. G.; Robertson, S. N.; Cameron, K.; Hough, J.; Salmeron-Sanchez, M.; Tsimbouri, P. M.; Vichare, P.; Dalby, M. J.; Reid, S. Design, Construction and Characterisation of a Novel Nanovibrational Bioreactor and Cultureware for Osteogenesis. *Sci. Rep.* **2019**, *9* (1), 12944.

(11) Abdelrahman, S.; Ireland, A.; Winter, E. M.; Purcell, M.; Coupaud, S. Osteoporosis after Spinal Cord Injury: Aetiology, Effects and Therapeutic Approaches. *J. Musculoskeletal Neuronal Interact.* **2021**, *21* (1), 26−50.

(12) Williams, J. A.; Huesa, C.; Turunen, M. J.; Oo, J. A.; Radzins, O.; Gardner, W.; Windmill, J. F. C.; Isaksson, H.; Tanner, K. E.; Riddell, J. S.; Coupaud, S. Time Course Changes to Structural, Mechanical and Material Properties of Bone in Rats after Complete

Spinal Cord Injury. *J. Musculoskeletal Neuronal Interact.* **2022**, *22* (2), 212−234.
(13) Cardinale, M.; Rittweger, J. Vibration Exercise Makes Your Muscles and Bones Stronger: Fact or Fiction? *J. Br. Menopause Soc.* **2006**, *12* (1), 12−18.
(14) Padilla, F.; Puts, R.; Vico, L.; Raum, K. Stimulation of Bone Repair with Ultrasound: A Review of the Possible Mechanic Effects. *Ultrasonics* **2014**, *54* (5), 1125−1145.
(15) Roll, J. P.; Vedel, J. P.; Ribot, E. Alteration of Proprioceptive Messages Induced by Tendon Vibration in Man: A Microneurographic Study. *Exp. Brain Res.* **1989**, *76* (1), 213.
(16) Harrison, A.; Lin, S.; Pounder, N.; Mikuni-Takagaki, Y. Mode & Mechanism of Low Intensity Pulsed Ultrasound (LIPUS) in Fracture Repair. *Ultrasonics* **2016**, *70*, 45−52.
(17) Matsumoto, K.; Shimo, T.; Kurio, N.; Okui, T.; Ibaragi, S.; Kunisada, Y.; Obata, K.; Masui, M.; Pai, P.; Horikiri, Y.; Yamanaka, N.; Takigawa, M.; Sasaki, A. Low-Intensity Pulsed Ultrasound Stimulation Promotes Osteoblast Differentiation through Hedgehog Signaling. *J. Cell. Biochem.* **2018**, *119* (6), 4352−4360.
(18) Tassinary, J. A. F.; Lunardelli, A.; Basso, B. d. S.; Dias, H. B.; Catarina, A. V.; Stülp, S.; Haute, G. V.; Martha, B. A.; Melo, D. A. d. S.; Nunes, F. B.; Donadio, M. V. F.; Oliveira, J. R. de. Low-Intensity Pulsed Ultrasound (LIPUS) Stimulates Mineralization of MC3T3-E1 Cells through Calcium and Phosphate Uptake. *Ultrasonics* **2018**, *84*, 290−295.
(19) Sun, S.; Sun, L.; Kang, Y.; Tang, L.; Qin, Y. X.; Ta, D. Therapeutic Effects of Low-Intensity Pulsed Ultrasound on Osteoporosis in Ovariectomized Rats: Intensity-Dependent Study. *Ultrasound Med. Biol.* **2020**, *46* (1), 108−121.
(20) Sun, S.; Tang, L.; Zhao, T.; Kang, Y.; Sun, L.; Liu, C.; Li, Y.; Xu, F.; Qin, Y. X.; Ta, D. Longitudinal Effects of Low-Intensity Pulsed Ultrasound on Osteoporosis and Osteoporotic Bone Defect in Ovariectomized Rats. *Ultrasonics* **2021**, *113*, 106360.
(21) Judex, S.; Lei, X.; Han, D.; Rubin, C. Low-Magnitude Mechanical Signals That Stimulate Bone Formation in the Ovariectomized Rat Are Dependent on the Applied Frequency but Not on the Strain Magnitude. *J. Biomech.* **2007**, *40* (6), 1333−1339.
(22) Lim, D.; Ko, C. Y.; Seo, D. H.; Woo, D. G.; Kim, J. M.; Chun, K. J.; Kim, H. S. Low-Intensity Ultrasound Stimulation Prevents Osteoporotic Bone Loss in Young Adult Ovariectomized Mice. *J. Orthop. Res.* **2011**, *29* (1), 116−125.
(23) Bramlett, H. M.; Dietrich, W. D.; Marcillo, A.; Mawhinney, L. J.; Furones-Alonso, O.; Bregy, A.; Peng, Y.; Wu, Y.; Pan, J.; Wang, J.; Guo, X. E.; Bauman, W. A.; Cardozo, C.; Qin, W. Effects of Low Intensity Vibration on Bone and Muscle in Rats with Spinal Cord Injury. *Osteoporosis Int.* **2014**, *25* (9), 2209−2219.
(24) Minematsu, A.; Nishii, Y.; Imagita, H.; Takeshita, D.; Sakata, S. Whole-Body Vibration Can Attenuate the Deterioration of Bone Mass and Trabecular Bone Microstructure in Rats with Spinal Cord Injury. *Spinal Cord* **2016**, *54* (8), 597−603.
(25) Warden, S. J.; Bennell, K. L.; Matthews, B.; Brown, D. J.; Mcmeeken, J. M.; Wark, J. D. Efficacy of Low-Intensity Pulsed Ultrasound in the Prevention of Osteoporosis Following Spinal Cord Injury. *Bone* **2001**, *29* (5), 431−436.
(26) Williams, J. A.; Huesa, C.; Windmill, J. F. C.; Purcell, M.; Reid, S.; Coupaud, S.; Riddell, J. S. Spatiotemporal Responses of Trabecular and Cortical Bone to Complete Spinal Cord Injury in Skeletally Mature Rats. *Bone Rep.* **2022**, *16*, 101592.
(27) Warden, S. J.; Bennell, K. L.; Forwood, M. R.; McMeeken, J. M.; Wark, J. D. Skeletal Effects of Low-Intensity Pulsed Ultrasound on the Ovariectomized Rodent. *Ultrasound Med. Biol.* **2001**, *27* (7), 989−998.
(28) Warden, S. J.; Bennell, K. L.; McMeeken, J. M.; Wark, J. D. Can. Conventional Therapeutic Ultrasound Units Be Used to Accelerate Fracture Repair? *Phys. Ther. Rev.* **1999**, *4* (2), 117−126.
(29) Naruse, K.; Mikuni-Takagaki, Y.; Urabe, K.; Uchida, K.; Itoman, M. Therapeutic Ultrasound Induces Periosteal Ossification without Apparent Changes in Cartilage. *Connect. Tissue Res.* **2009**, *50* (1), 55−63.
(30) Greenleaf, J. F.; Kinnick, R.; Bolander, M. Ultrasonically Induced Motion in Tissue during Fracture Treatment? *Ultrasound Med. Biol.* **2003**, *29* (5), S157−S158.
(31) Argadine, H. M.; Kinnick, R. R.; Bolander, M. E.; Greenleaf, J. F. 1 kHz Low Power Sound Stimulates ATDC5 Chondrocytes. *Proc. - IEEE Ultrason. Symp.* **2005**, *2*, 996−998.
(32) Argadine, H. M.; Bolander, M. E.; Greenleaf, J. F. Stimulation of Proteoglycan Synthesis with Low-Intensity 1 kHz Vibration. *Proc. - IEEE Ultrason. Symp.* **2006**, *1*, 849−851.
(33) Marvel, S.; Okrasinski, S.; Bernacki, S. H.; Loboa, E.; Dayton, P. A. The Development and Validation of a LIPUS System with Preliminary Observations of Ultrasonic Effects on Human Adult Stem Cells. *IEEE Trans. Ultrason. Eng.* **2010**, *57* (9), 1977−1984.
(34) Thompson, D. D.; Simmons, H. A.; Pirie, C. M.; Ke, H. Z. FDA Guidelines and Animal Models for Osteoporosis. *Bone* **1995**, *17* (4), 125S−133S.
(35) Rauch, F.; Sievanen, H.; Boonen, S.; Cardinale, M.; Degens, H.; Felsenberg, D.; Roth, J.; Schoenau, E.; Verschueren, S.; Rittweger, J. Reporting Whole-Body Vibration Intervention Studies: Recommendations of the International Society of Musculoskeletal and Neuronal Interactions. *J. Musculoskeletal Neuronal Interact.* **2010**, *10* (3), 193−198.
(36) Kiiski, J.; Heinonen, A.; Järvinen, T. L.; Kannus, P.; Sievänen, H. Transmission of Vertical Whole Body Vibration to the Human Body. *J. Bone Miner. Res.* **2008**, *23* (8), 1318−1325.
(37) Shields, R. K.; Dudley-Javoroski, S. Musculoskeletal Adaptations in Chronic Spinal Cord Injury: Effects of Long-Term Soleus Electrical Stimulation Training. *Neurorehabilitation Neural Repair* **2007**, *21* (2), 169−179.
(38) Dudley-Javoroski, S.; Petrie, M. A.; McHenry, C. L.; Amelon, R. E.; Saha, P. K.; Shields, R. K. Bone Architecture Adaptations after Spinal Cord Injury: Impact of Long-Term Vibration of a Constrained Lower Limb. *Osteoporosis Int.* **2016**, *27* (3), 1149−1160.
(39) Roberts, B. C.; Giorgi, M.; Oliviero, S.; Wang, N.; Boudiffa, M.; Dall'Ara, E. The Longitudinal Effects of Ovariectomy on the Morphometric, Densitometric and Mechanical Properties in the Murine Tibia: A Comparison between Two Mouse Strains. *Bone* **2019**, *127*, 260−270.
(40) Williams, J. A.; Windmill, J. F. C.; Tanner, K. E.; Riddell, J. S.; Coupaud, S. Global and Site-Specific Analysis of Bone in a Rat Model of Spinal Cord Injury-Induced Osteoporosis. *Bone Rep.* **2020**, *12*, 100233.
(41) Bouxsein, M. L.; Boyd, S. K.; Christiansen, B. A.; Guldberg, R. E.; Jepsen, K. J.; Müller, R. Guidelines for Assessment of Bone Microstructure in Rodents Using Micro-Computed Tomography. *J. Bone Miner. Res.* **2010**, *25* (7), 1468−1486.
(42) Domander, R.; Felder, A. A.; Doube, M. BoneJ2 - Refactoring Established Research Software. *Wellcome Open Res.* **2021**, *6*, 37.
(43) Harrigan, T. P.; Mann, R. W. Characterization of Microstructural Anisotropy in Orthotropic Materials Using a Second Rank Tensor. *J. Mater. Sci.* **1984**, *19*, 761−767.
(44) Wagner, D. W.; Lindsey, D. P.; Beaupre, G. S. Deriving Tissue Density and Elastic Modulus from MicroCT Bone Scans. *Bone* **2011**, *49* (5), 931−938.
(45) Turner, C.; Burr, D. Basic Biomechanical Measurements of Bone: A Tutorial. *Bone* **1993**, *14* (4), 595−608.


https://doi.org/10.1021/acsnano.4c02104
*ACS Nano* 2024, 18, 17630−17641